Panretinal handheld OCT angiography for pediatric retinal imaging

SHUIBIN NI,[1,2] GUANGRU BEN LIANG,[1,2] RINGO NG,[1] SUSAN OSTMO,[1] YALI JIA,[1,2] MICHAEL F. CHIANG,[3,4] DAVID HUANG,[1,2] ALISON H. SKALET,[1,5,6,7] BENJAMIN K. YOUNG,[1] J. PETER CAMPBELL,[1] AND YIFAN JIAN[1,2,*]

[1]*Casey Eye Institute, Oregon Health & Science University, Portland, OR, 97239, USA*
[2]*Department of Biomedical Engineering, Oregon Health & Science University, Portland, OR, 97239, USA*
[3]*National Eye Institute, National Institutes of Health, Bethesda, MD, 20892, USA*
[4]*National Library of Medicine, National Institutes of Health, Bethesda, MD, 20892, USA*
[5]*Knight Cancer Institute, Oregon Health & Science University, Portland, OR, 97239, USA*
[6]*Department of Radiation Medicine, Oregon Health & Science University, Portland, OR, 97239, USA*
[7]*Department of Dermatology, Oregon Health & Science University, Portland, OR, 97239, USA*
**jian@ohsu.edu*

Abstract: Comprehensive visualization of retina morphology is essential in the diagnosis and management of retinal diseases in pediatric populations. Conventional imaging techniques often face challenges in effectively capturing the peripheral retina, primarily due to the limitations in current optical designs, which lack the necessary field of view to characterize the far periphery. To address this gap, our study introduces a novel ultra-widefield optical coherence tomography angiography (OCTA) system. This system, specifically tailored for pediatric applications, incorporates an ultrahigh-speed 800 kHz swept-source laser. The system's innovative design achieves a 140° field of view while maintaining excellent optical performance. Over the last 15 months, we have conducted 379 eye examinations on 96 babies using this system. It demonstrates marked efficacy in the diagnosis of retinopathy of prematurity, providing detailed and comprehensive peripheral retinal angiography. The capabilities of the ultra-widefield handheld OCTA system in enhancing the clarity and thoroughness of retina vascularization assessments have significantly improved the precision of diagnoses and the customization of treatment strategies. Our findings underscore the system's potential to advance pediatric ophthalmology and broaden the scope of retinal imaging.

1. Introduction

Optical coherence tomography (OCT), especially with the integration of OCT angiography (OCTA), has instigated a significant shift in ophthalmology, offering high-resolution, cross-sectional retinal images and enhancing diagnostic capabilities [1,2]. Ultra-widefield imaging in OCT/OCTA has become an invaluable tool, providing detailed views of both the central and peripheral retina, improving management of complex ocular conditions in pediatric patients [3–5]. Traditional OCT/OCTA systems, primarily desktop models, however, have limitations in pediatric retinal examinations due to difficulties in imaging non-cooperative infants [6,7]. In response to these challenges, there have been explorations into handheld OCT prototypes for pediatric patient imaging [3,8–13]. Yet, these prototypes typically face limitations in extending the imaging area to the retinal periphery, a constraint largely attributed to the size and weight limitations of portable probe design, which in turn diminishes their clinical utility. Furthermore, the restricted imaging speed of these systems presents a barrier to the practical implementation of OCTA.

Retinopathy of prematurity (ROP) is a leading cause of childhood blindness worldwide. This vasoproliferative disorder is characterized by progressive fibrovascular changes in both the posterior pole and the retinal periphery [3,14,15]. Identifying and classifying changes in the retinal vasculature are crucial for early and accurate diagnosis, serving as key indicators for treatment strategies [16]. Timely and precise diagnosis can make ROP treatment highly effective, significantly reducing the risk of blindness associated with the condition [17–20]. The current standard for ROP management includes regular (weekly or bi-weekly) dilated binocular indirect ophthalmoscopy examinations with scleral depression and/or widefield digital fundus imaging (WDFI). However, ophthalmoscopic examinations can be subjective, with scleral depression specifically causing significant neonatal stress, and WDFI may have variable image quality and contrast for definitive ROP diagnosis. Handheld OCT may offer a more objective alternative for ROP detection. Additionally, ROP examinations pose medical risks for fragile neonates, including increased cardiopulmonary complications [21]. Therefore, methods that reduce examination duration and frequency could substantially benefit this patient group.

To overcome these obstacles, we introduced an innovative panretinal ultrahigh-speed handheld swept-source OCTA system, tailored for pediatric use. This system is engineered to facilitate faster, more thorough, and less stressful examinations, specifically benefiting pediatric patients. Equipped with an 800 kHz swept-source laser, the system utilizes a contact-based approach that effectively reduces alignment time and enhances image quality. A notable feature of this system is its ability to achieve a 140° field of view (FOV, visual angle measured from the pupil plane) while preserving superior optical performance. This attribute facilitates precise, panoramic visualization of the retina, which is integral for detailed structural examination and the accurate detection of neovascularization, thereby enriching the scope and efficacy of retinal assessments.

2. Methods

2.1 System setup

The schematic diagram of the proposed panretinal ultrahigh-speed handheld OCTA system is shown in **Fig. 1**. Building upon our previously developed system [22–24], we have refined the optical design of the probe, achieving a 140° FOV with superior optical performance. The system incorporates a swept-source laser, operating at an 800 kHz A-scan rate and a central wavelength of 1060 nm. The employed vertical-cavity surface-emitting laser (VCSEL) (Thorlabs, Inc., USA) has a 70 nm (6 dB) tuning range, yielding an axial resolution of 7.06 μm in air. Notably, the laser operates with a bidirectional sweep at 100% duty cycle, providing an average output power of approximately 40 mW. The high output power of the VCSEL laser was pivotal in optimizing the fiber-based interferometer. This optimization ensured the delivery of a sufficient yet safe amount of imaging beam power to the patient's eye while maximizing collection efficiency. The system retains the 4-coupler interferometer configuration, comprising two 25/75 fiber couplers [FC1/FC4 in **Fig. 1**] and two 50/50 fiber couplers [FC2/FC3 in **Fig. 1**]. This arrangement allows for 25% of the power from FC4 to be delivered to the probe, which then collects 75% of the signal reflected from the sample. The handheld probe's output power is maintained at 4.75 mW, adhering to safety standards without posing any light hazard, as per ANSI Z80.36-2021.

Polarization state variation in the optical fiber patch cord within the sample arm during the alignment can impact the OCT signal-to-noise ratio due to polarization mismatch between the sample and reference arms. To address this, a two-paddle motorized fiber polarization controller (MPC220, Thorlabs Inc., USA) was installed in the reference arm's path. Automated polarization state matching, based on the target *en face* image brightness, is performed before imaging sessions [22]. Additionally, a linear stage (X-LHM100A-E03, Zaber Technologies Inc., Canada), featuring a 100 mm travel range, is integrated to adjust the optical delay for imaging neonates with varying eye axial length.

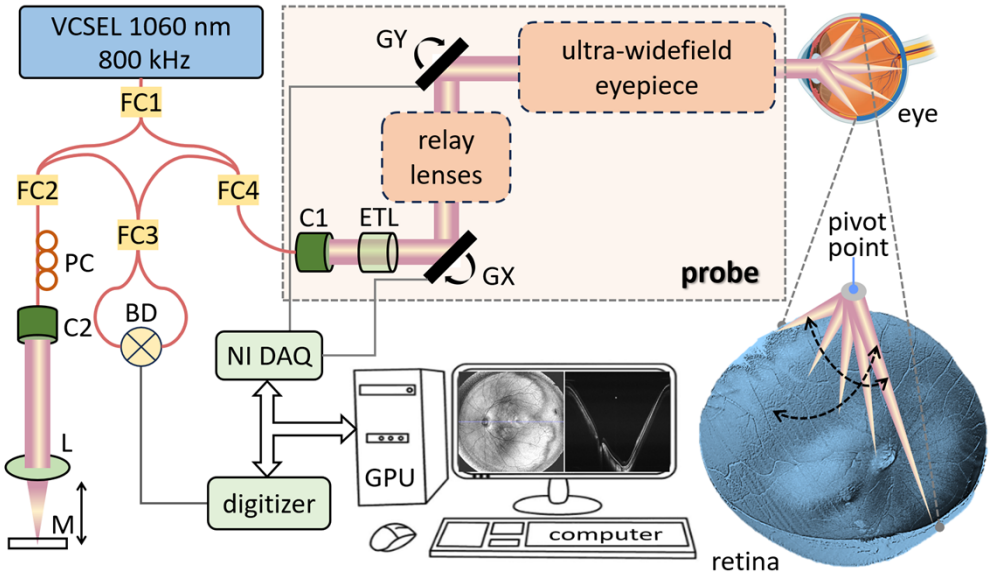

Fig. 1. Illustrative diagram of the proposed panretinal ultrahigh-speed handheld OCTA system. The orange dashed box at the top center illustrates the elements integrated into the portable probe. The lens group between the GX and GY is an ultra-compact telecentric relay lens system. The lens group between the GY and eye is the ultra-widefield eyepiece composed of off-the-shelf lenses. The right bottom corner represents the scanning beam on the 3D volume rendering retina. Key components include: C1/C2: collimators; L: lens; ETL: electronically tunable lens; GX/GY: the fast/slow axes of the galvanometer scanners; M: mirror; PC: polarization controller; FC1-FC4: fiber couplers; BD: balanced detector; VCSEL: vertical-cavity surface-emitting laser; GPU: graphics processing unit. Red lines illustrate fiber optics. Grey lines represent the electrical cables transmitting digital signals.

2.2 Portable probe optical setup

The optical design of the portable probe was developed and optimized using Zemax OpticStudio software (Ansys Inc., USA). The design with ray tracing [as depicted in **Figs. 2(A) and 2(B)**] encompasses an ultra-compact telecentric relay lens system and an ultra-widefield eyepiece. The relay lens group, positioned between the fast galvanometer scanner (GX) and the slow galvanometer scanner (GY), ensures collimated light transmission with minimal beam deviation across both scanner planes. The ultra-widefield eyepiece, integral for attaining an extended FOV, is composed of a series of selected off-the-shelf lenses.

The block diagram of the custom-designed telecentric relay lens system is illustrated in **Fig. 2(E)**. The lens details in the relay lens system are listed in **Table 1**. The telecentric relay lens system is critical for correcting optical misalignment during 2-dimensional scanning. Typically, the two orthogonal scanners are placed 5-10 mm to each other. Because of this separation distance, the imaging beam position on the pupil plane when scanned at different angles cannot be overlapped. By separating the two scanners with a relay lens system, the two scanners are optically conjugated [22,24,25]. However, it is observed that the traditional relay lens design, using off-the-shelf optics, has not reached an optimal level of performance. The comparative results of the beam wandering on the GY plane was shown in **Fig. 2(D)**. The result reveals that in the traditional design, there is a notable 7.25% offset in the beam wandering on the GY plane during scanning. In contrast, the custom-designed telecentric relay lens system demonstrates a significantly reduced offset of only 1.07%, indicating a marked improvement in alignment. The custom-design telecentric relay lens system incorporates two identical doublet lenses [L1/L2 and L7/L8 as shown in **Fig. 1(E)**] and two pairs of matching singlet lenses [L3/L6 and L4/L5 in **Fig. 1(E)**]. The doublet lenses consist of a negative meniscus lens paired with a biconvex lens. The custom-designed telecentric relay lens system with ultra-compact dimensions [20 mm

in diameter and 76 mm in length as shown in **Fig. 2**(**F**)], was manufactured by Avantier Inc., USA. These lenses create an optical conjugation between the GX and the GY. The configuration ensures the footprints on both GX and GY are perfectly aligned, thereby partly addressing the iris vignetting artifact.

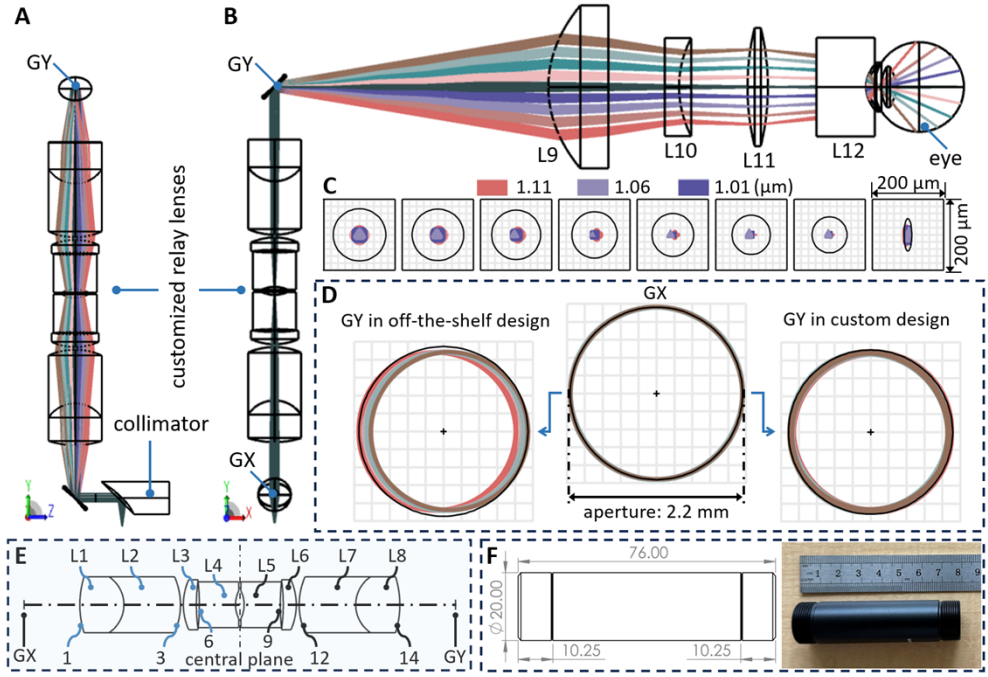

Fig. 2. Detailed optical design of the portable probe. (**A**) The side view showcases the 3D configuration of the telecentric relay lens system in OpticStudio. (**B**) The front view displays the 3D arrangement of the whole sample arm in OpticStudio. L9-L11: off-the-shelf lenses from Edmund Optics Inc.; L12: Quad Pediatric lens from VOLK Optical Inc. (**C**) Optical performance on the retinal plane of a simulated eye model covering from a field of view ranging from 0° to 140° at 20° intervals. The black circles represent the Airy disk, with a central Airy radius of 73.6 μm. Notably, as the scanning angle extends towards the periphery, the incident beam's shape transitions from circular to elliptical form on the pupil plane, causing variations in the Airy disk size with increasing scanning beam angles. Scale markers are set at 200 μm. Color coding for the wavelength: red: 1100 nm; light purple: 1060 nm; dark purple: 1010 nm. (**D**) Comparison of scanning beam footprint diagrams on the GY, contrasting beams relayed by the traditional design using off-the-shelf lenses [22,24] with those of the proposed custom design. (**E**) The block diagram of the telecentric relay lens system. The lens details are listed in **Table 1**. (**F**) On the left: the mechanical configuration of the relay lenses. On the right: a photograph of the actual relay lenses produced. All dimensions are provided in millimeters.

The ultra-widefield eyepiece lens system, located between the GY and eye, features a compact, lightweight design, ensuring an appropriate working distance to align with the iris plane when the contact surface is placed on the cornea. The ultra-widefield eyepiece includes an aspheric lens [L9 in **Fig. 2**(**B**)] with a 40 mm focal length (17-008, Edmund Optics Inc., USA), a plano-concave lens [L10 in **Fig. 2**(**B**)] with a -50 mm focal length (68-001, Edmund Optics Inc., USA), and a double-convex lens [L11 in **Fig. 2**(**B**)] with a 60 mm focal length (67-661, Edmund Optics Inc., USA). Additionally, a specialized contact lens (Quad Pediatric, VOLK Optical Inc., USA) was incorporated. The Quad Pediatric lens [L12 in **Fig. 2**(**B**)] combines an advanced double aspheric lens and a meniscus lens, further enhanced with a custom anti-reflection coating. The coating, tailored to reduce reflectivity below 0.5% within the 950 nm to 1150 nm wavelength range, significantly improves sample light collection efficiency [23,24]. **Figure 2**(**C**) depicts a set of point spread functions (PSFs) corresponding to

the ray traces from **Figs. 2(A) and 2(B)**, representing a FOV ranging from 0° to 140° at 20° intervals. These PSF plots demonstrate diffraction-limited performance across the entire FOV at all wavelength ranges. However, the complex double aspherical ocular lens in L12 introduces some irregularities in the beam profile on the retina as the scanning angle extends towards the periphery. This effect can influence the size and shape of the PSF, and consequently, the size of the Airy disk in the spot diagram varies with the increasing FOV. Upon demagnification by the ultra-widefield eyepiece, the beam size on the pupil plane was measured at 0.35 mm. This results in a theoretical spot size of 46.4 μm (measured as the $1/e^2$ diameter) on the retinal plane, specifically when imaging an infant with an axial eye length of 17 mm.

Table 1. Lens data of the ultra-compact telecentric relay lens system

Surface	Radius/mm	Thickness/mm	Material (Lens)
1	21.843	10.226	H-LAK7A (L1)
2	-7.812	13.108	H-ZF73GT (L2)
3	-16.059	0.676	
4	14.188	3.023	H-ZLAF92 (L3)
5	42.219	0.676	
6	-54.979	8.391	H-ZF39 (L4)
7	7.229	2	
8	-7.229	8.391	H-ZF39 (L5)
9	54.979	0.676	
10	-42.219	3.023	H-ZLAF92 (L6)
11	-14.188	0.676	
12	16.059	13.108	H-ZF73GT (L7)
13	7.812	10.226	H-LAK7A (L8)
14	-21.843	12.900	

2.3 Portable probe mechanical setup and system assembly

The simulation results from the optimized Zemax analysis were transferred into CAD software (SolidWorks, Dassault Systèmes, France) to develop the mechanical design. This integration facilitated the precision alignment of the lens system, achieved using custom-design lens tubes [illustrated as gray components within the red dashed box in **Fig. 3**(**A**)]. Additionally, a 5.5-inch AMOLED display with two separate imaging windows [**Figs. 3**(**B**)-**3**(**D**)], facilitating the alignment process. For robust protection and organization, the optical fiber, and various electrical cables, including galvo cable sets, electronically tunable lens driver cable, HDMI cable for the display, and Micro-USB cable for display power, were bundled within a nylon protective sleeve sheath.

The OCT engine of the imaging system was encased in a 19-inch rack enclosure, spanning 3 rack units (U) in height (EC3U, Thorlabs Inc., USA), while the electrical components were housed in a separate 2U 19-inch rack enclosure. These enclosures were then integrated into a portable OCT imaging cart, with the complete assembly presented in **Fig. 3**(**A**). To enhance operational efficiency, a secondary keyboard, programmed with six shortcut keys for functions such as data saving, scanning mode toggling, auto-focus, auto-polarization control, and reference arm length adjustment, was connected to the system. This design choice streamlined the operation process, reducing reliance on traditional mouse-based controls and thereby increasing operation efficiency.

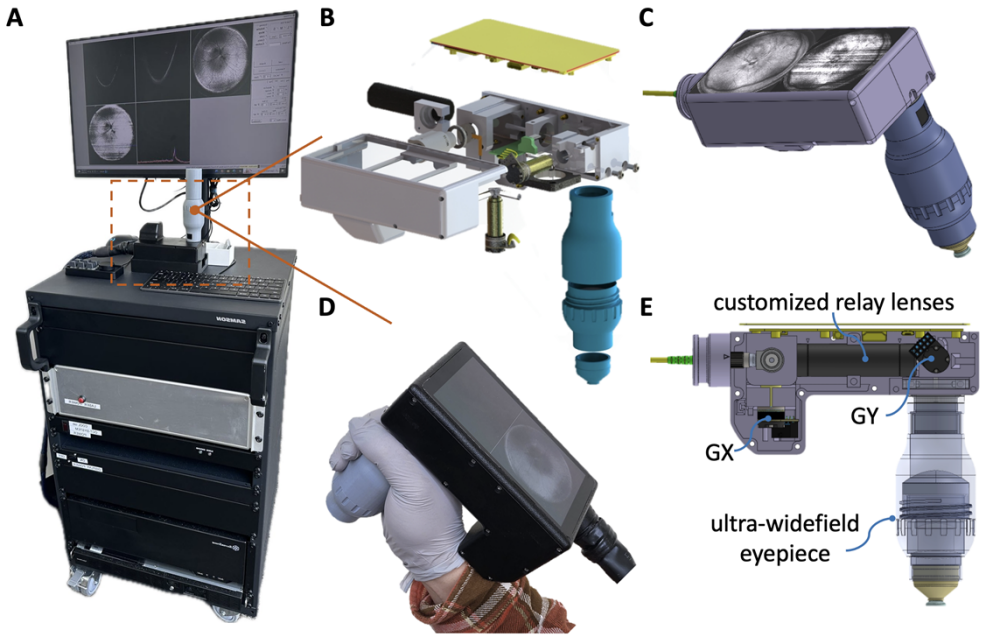

Fig. 3. Integrated system and portable probe assembly. (**A**) Photograph showcasing the assembly panretinal handheld OCTA system. (**B**) Exploded view detailing the mechanical design of the probe. (**C**) 3D mechanical designs of the fully assembled portable probe. (**D**) Photographic depiction of the fully assembled portable probe. (**E**) Front view of the 3D mechanical design, showing key internal components of the probe.

2.4 Scanning protocol and data visualization

In this project, we implemented three separate scanning protocols to meet imaging requirements. The first was a high-speed alignment mode operating at a volume rate of 10 Hz, designed for rapid identification and alignment of the target area. For high resolution data acquisition, we employed two modes: an OCT mode for retinal structure imaging and an OCTA mode for angiographic volume capture. In the OCT mode, the protocol involved 800 A-scans per B-scan and 800 B-scans per volume, enabling a rapid volume acquisition in just 0.8 seconds. In contrast, the OCTA mode's protocol incorporated three repeated B-scans at each location, with 800 A-scans per B-scan, resulting in a total of 2400 B-scans per volume acquired in 2.4 seconds.

Both OCT and OCTA images were captured and processed using our custom-developed software, OCTViewer. This software was GPU-accelerated, facilitating real-time quality feedback and alignment processes [26–28]. Peripheral hardware controls, such as a motorized polarization controller, electronically tunable lens, and motorized reference arm, were integrated into the software package. The increased imaging speed for ultra-widefield OCTA necessitates a high-speed digitizer and generates substantial data volumes. In our 800 kHz OCTA system, each OCTA volume generates approximately 16 GB of unprocessed raw data.

OCTA B-scans were generated using the split-spectrum amplitude-decorrelation algorithm [29]. The algorithm was applied to three repeated B-scans at each specific retinal location, enhancing the accuracy and reliability of the acquired data. The generation of *en face* OCTA images commenced with automated segmentation of retinal layers, followed by manual adjustment to improve segmentation accuracy. For further processing of the *en face* OCTA images, a median subtraction technique was employed to reduce the presence of minor artifacts, which are commonly encountered in pediatric imaging. After median subtraction, a Gabor filter was applied to each image to enhance the OCTA signal by emphasizing key image features

while reducing background noise [30,31]. In the final processing step, a 'hot' color mapping was utilized for each *en face* image to improve visual interpretability.

2.5 Study subjects

The panretinal handheld OCTA system was employed for imaging infants in both the operating room and the neonatal intensive care unit (NICU). Pediatric patients for this study were enrolled from the Casey Eye Institute at the Oregon Health & Science University (OHSU) from September 2022 to January 2024. The research was conducted under the approval of the OHSU Institutional Review Board (IRB)/Ethics Committee, in strict compliance with the ethical guidelines outlined in the Declaration of Helsinki. Before initiating any study-related procedures, written informed consent was obtained from the parents or legal guardians of each infant participant, confirming their consent for their child's involvement in this imaging study. As per routine ROP examination, before each imaging session, infants were administered cyclopentolate hydrochloride and phenylephrine hydrochloride in both eyes. Then a standard pediatric speculum was placed [illustrated by green arrows in **Fig. 4**(**A**)], and lubricant eye gel (Systane, Alcon, Switzerland) was instilled onto the corneal surface, to prevent corneal abrasion and ensure coupling between the lens meniscus and cornea. During the imaging, the operator precisely controlled the pressure exerted on the eyeball by gently resting a hand on the infant's forehead.

3. Results

Over 15 months, we have conducted 379 eye examinations on 96 babies utilizing the imaging system. Each imaging session was streamlined to conclude within 2 minutes, which was crucial to minimize the discomfort of the patients and mitigate medical risks. Representative *en face* OCT images obtained during these pediatric examinations are illustrated in **Fig. 4**. The system's high-speed alignment mode, equipped with real-time visualization, functions comparable to a fundus camera. Its deep depth of focus is instrumental in accurately locating the target area. For instance, **Fig. 4**(**A**) displays an *en face* OCT image captured from the orbital area of an infant before the placement of the probe on the cornea. The OCT mode, with its rapid visualization capabilities (0.8 seconds), effectively minimizes the appearance of motion artifacts, as depicted in **Figs. 4**(**B**) and **4**(**C**). By adjusting the probe incident angle appropriately, we successfully visualized the ciliary body and ora serrata, which were considered the peripheral limits of the retina. Notably, these images were acquired without the necessity for scleral depression.

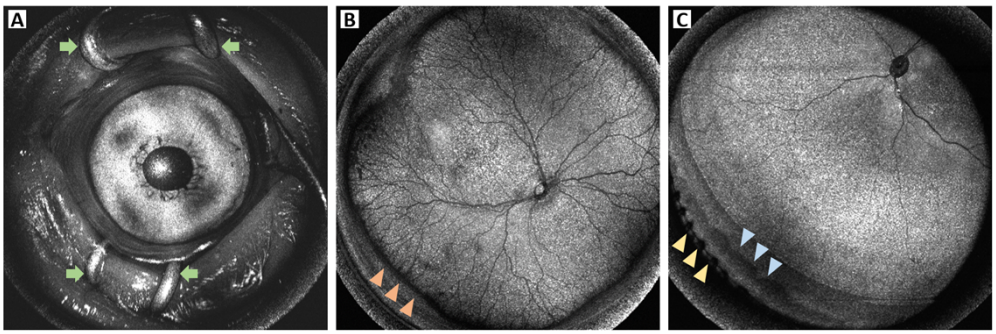

Fig. 4. Representative *en face* OCT images from ROP examinations. (**A**) *En face* OCT image displaying the orbital region of an infant during the alignment process, with green arrows indicating the eye speculum used to keep the eyelids open and expose the ocular surface. (**B**) *En face* OCT image from an infant (born at 24 weeks gestation, 568 grams, and imaged at 35 weeks postmenstrual age) diagnosed with ROP zone II, stage 2, showing extraretinal neovascular proliferation at the retinal vascular-avascular junction (marked by red arrowheads). This proliferation was almost entirely captured around the retinal periphery into zone II in a single, non-montage image. (**C**) *En face* OCT image from an infant (born at 29 weeks gestation, 1344 grams, and imaged at 39 weeks postmenstrual age), showcasing the ability to capture the ora

serrata (indicated by blue arrowheads) and the ciliary body (highlighted by yellow arrowheads), without scleral depression.

Incorporating OCTA into our imaging system has significantly advanced our capability to delineate the vascular-avascular boundary in ROP. The feature proves particularly beneficial in scenarios where the fibrovascular ridge is not readily apparent during clinical evaluations or via structural *en face* OCT imaging. The *en face* OCTA image showcases the junction with greater clarity and definition compared to the *en face* OCT structural image, as indicated by green arrowheads in **Figs. 5**(**A**) and **5**(**B**). Such delineation is imperative for determining the extent of retina vascularization, a task that is challenging with ophthalmoscopy in the absence of disease.

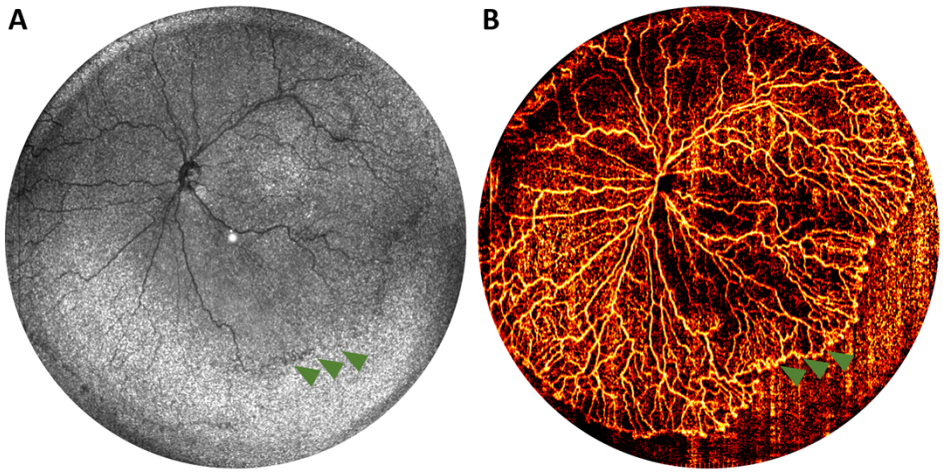

Fig. 5. (**A**) *En face* OCT image of the right eye from an infant (born at 23 weeks gestation, 593 grams, and imaged at 38 weeks postmenstrual age) with ROP stage 1, where the fibrovascular ridge is marked by green arrowheads but is not distinctly visible in the structural *en face* image. (**B**) The corresponding *en face* OCTA image, revealing the vascularized retina with greater clarity.

Neovascularization plays a pivotal role in the progression of ROP. During the ROP stage 2, as depicted in **Fig. 6**(**A**), there is a proliferation of abnormal blood vessels at the junction of the vascular and avascular regions of the retina. The *en face* OCTA can effectively illustrate the neovascularization by projecting flow signals located within the vitreous, particularly from the slab positioned above the inner limiting membrane. As demonstrated in **Fig. 6**(**B**), neovascularization in ROP extends beyond the ridge area. Previously, visualizing and quantifying these vascular changes posed significant challenges. However, advancements in imaging techniques may now enhance our understanding of the phenotypic patterns of ROP progression and its underlying physiological processes [32].

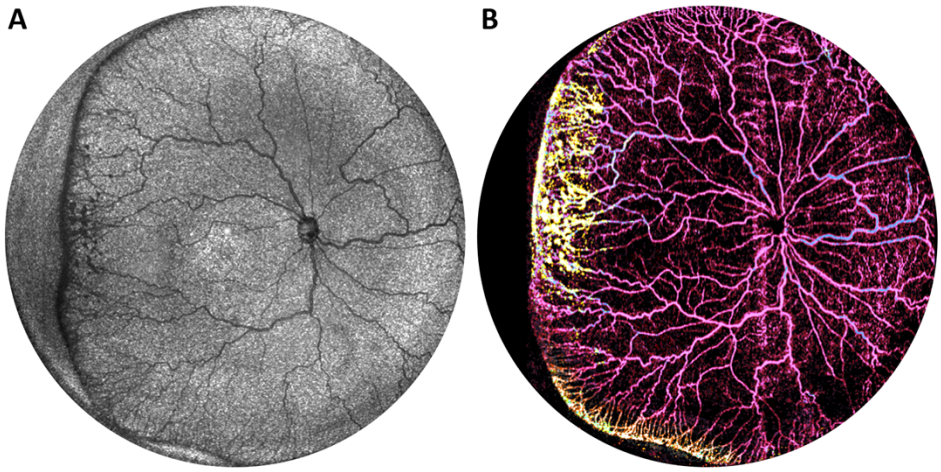

Fig. 6. (**A**) *En face* OCT image of the left eye from the same infant as in **Fig. 5**, presenting with ROP stage 2. (**B**) The corresponding *en face* OCTA image, illustrating the area of neovascularization, distinguished by yellow vessels.

4. Discussion

The imaging of the peripheral retina poses a considerable challenge, especially in pediatric populations. Existing retinal imaging devices, are primarily designed for adults, require high levels of patient cooperation, and are not ideally configured for pediatric use. Handheld WDFI systems have gained popularity in managing pediatric retinal diseases owing to their portability, but often compromise on image contrast and resolution. Standard OCT retinal imaging systems typically do not offer an imaging FOV exceeding 100°, limited by optical design, imaging speed limitations, and axial range. There is a critical demand for a dedicated, portable, handheld OCT retina scanner for pediatric applications. Several research groups, including ours, have been pioneering the development of faster OCT prototypes optimized for neonatal use. We are the only group to have successfully achieved ultra-widefield OCT imaging in non-sedated babies [23,24,33]. Our previously reported panretinal OCT imaging system, notable for its extensive FOV in a single capture, has proven effective in diagnosing various pediatric retinal diseases. It has facilitated sophisticated analyses of peripheral pathologies, uncovering previously unknown relationships, such as the correlation between peripheral fibrovascular ridge thickness and ROP stage classification [16,34].

Our earlier systems encountered challenges such as limited imaging speed and suboptimal optical design, which impeded the integration of OCTA mode in ultrawide imaging [23,24,35]. In this study, however, we have addressed these limitations by developing a faster OCT engine with improved optical performance. This has enabled the first successful implementation of ultra-widefield OCTA in premature infants. Compared to WFDI, our novel system offers a significantly larger FOV and enhanced image contrast, effectively highlighting peripheral pathologies. Our results demonstrate that the panretinal ultrahigh-speed handheld OCTA system could be helpful in understanding vascular growth dynamics in ROP.

Despite these advancements, our handheld OCTA system faces limitations. The contact imaging method necessitates skilled ophthalmic technicians for image acquisition, though this is similar to current WDFI systems. Although the scanning pivot point is pre-set to minimize vignetting artifacts, the lens design with a predetermined curvature and working distance cannot accommodate the rapid growth of the eyes in premature infants. Additionally, a long axial imaging range is essential to avoid aliasing, due to the time constraints in imaging uncooperative infants, we sometimes cannot precisely adjust the reference arm to match the axial eye length. Furthermore, the optical performance at most scanning angles is near or at the

diffraction limit at the focal spot with a central radius of 73.6 µm. Increasing the beam size on the pupil in theory would improve transverse resolution for OCTA. However, this requires the integration of a larger aperture galvanometer scanner along with improvement in the optical design. A key consideration is that larger aperture galvanometer scanners have limited scanning speed, and an alternative scanning pattern might be required [36,37]. Moreover, an increase in numerical aperture could inadvertently compromise transverse resolution unless the optical design is thoroughly optimized. We conducted an optical simulation with a beam size triple that of the proposed system. This adjustment resulted in an improved central radius of the Airy disk, decreasing from 73.6 µm to 24.5 µm. However, the simulated spot diagram demonstrated a deterioration, as depicted in **Fig. 7**. An enhanced optical design aimed at minimizing optical aberrations at larger scanning angles is imperative; meanwhile it should not result in a significantly heavier or bulkier system. Finally, retinal layer segmentation algorithms are not yet optimized for current ultra-widefield OCTA images [38,39]. Future work should focus on optimizing these algorithms. Addressing these limitations and enhancing the current system's capabilities will further improve the utilities of ultra-widefield handheld OCTA in pediatric retinal imaging.

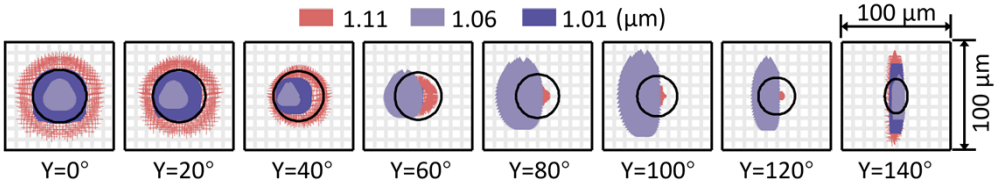

Fig. 7. Optical performance evaluation with a beam size tripled compared to the proposed system) on the retinal plane covering from a field of view ranging from 0° to 140° at 20° intervals, utilizing the same settings in OpticStudio as in **Fig. 2**. Scale markers are 100 µm. Wavelengths are color-coded as follows: red for 1100 nm, light purple for 1060 nm, and dark purple for 1010 nm.

5. Conclusion

We have successfully developed a panretinal ultrahigh-speed handheld swept-source OCTA system, specifically designed for pediatric retinal imaging. The advanced system incorporates an 800 kHz VCSEL laser source and can deliver an extensive 140° FOV. Its exceptional imaging proficiency, especially in capturing detailed peripheral retinal angiography, has demonstrated significant clinical value in the diagnosis of ROP. The system's broadened FOV enables clinicians to identify and evaluate various retinal pathologies, which might otherwise remain undetected in the periphery. Advanced technology provides essential insights for the accurate assessment and diagnosis of a range of ocular conditions affecting this critical eye region. Its application in pediatric ophthalmology is particularly beneficial, as early detection of retinal disorders can significantly influence the course of treatment and overall prognosis.

Acknowledgements. We would like to thank Professor Dr. Herbert Gross from Friedrich Schiller University Jena for his in-depth discussion on the optimization of relay lens design, and to Dr. Atriya Ghosh from Volk Optical, Inc., for his valuable insights into optical design.

Funding. National Institutes of Health (P30 EY010572, R01 HD107494, and R01 EY023285); Research to Prevent Blindness (Unrestricted departmental funding grant & Career Advancement Award); Bright Focus Foundation, and in part by the intramural research program of the National Eye Institute, NIH.

Disclosures. YaJ: Genentech (F, P); Optovue/Visionix (P, R), Optos (P). DH: Visionix (F, P, R); Genentech (P, R); Intalight (F); Canon (F); Cylite (F). All other authors declare they have no competing interests.

Data availability. Data underlying the results presented in this paper are not publicly available at this time but may be obtained from the authors upon reasonable request.

References

1. D. Huang, E. A. Swanson, C. P. Lin, J. S. Schuman, W. G. Stinson, W. Chang, M. R. Hee, T. Flotte, K. Gregory, C. A. Puliafito, and J. G. Fujimoto, "Optical Coherence Tomography," Science (1979) **254**(5035), 1178–1181 (1991).
2. J. G. Fujimoto, E. A. Swanson, and D. Huang, "Optical Coherence Tomography—History, Evolution, and Future Prospects," JAMA **330**(15), 1427 (2023).
3. J. P. Campbell, E. Nudleman, J. Yang, O. Tan, R. V. P. Chan, M. F. Chiang, D. Huang, and G. Liu, "Handheld optical coherence tomography angiography and ultra-wide-field optical coherence tomography in retinopathy of prematurity," JAMA Ophthalmol **135**(9), 977–981 (2017).
4. T.-T. P. Nguyen, S. Ni, S. Khan, X. Wei, S. Ostmo, M. F. Chiang, Y. Jia, D. Huang, Y. Jian, and J. P. Campbell, "Advantages of Widefield Optical Coherence Tomography in the Diagnosis of Retinopathy of Prematurity," Front Pediatr **9**, (2022).
5. T.-T. P. Nguyen, S. Ni, G. Liang, S. Khan, X. Wei, A. Skalet, S. Ostmo, M. F. Chiang, Y. Jia, D. Huang, Y. Jian, and J. P. Campbell, "Widefield Optical Coherence Tomography in Pediatric Retina: A Case Series of Intraoperative Applications Using a Prototype Handheld Device," Front Med (Lausanne) **9**, 860371 (2022).
6. J. P. Kolb, T. Klein, C. L. Kufner, W. Wieser, A. S. Neubauer, and R. Huber, "Ultra-widefield retinal MHz-OCT imaging with up to 100 degrees viewing angle," Biomed Opt Express **6**(5), 1534 (2015).
7. N. Choudhry, J. Golding, M. W. Manry, and R. C. Rao, "Ultra-Widefield Steering-Based Spectral-Domain Optical Coherence Tomography Imaging of the Retinal Periphery," Ophthalmology **123**(6), 1368–1374 (2016).
8. J. D. Malone, M. T. El-Haddad, S. S. Yerramreddy, I. Oguz, and Y. K. K. Tao, "Handheld spectrally encoded coherence tomography and reflectometry for motion-corrected ophthalmic optical coherence tomography and optical coherence tomography angiography," Neurophotonics **6**(04), 1 (2019).
9. C. Viehland, X. Chen, D. Tran-Viet, M. Jackson-Atogi, P. Ortiz, G. Waterman, L. Vajzovic, C. A. Toth, and J. A. Izatt, "Ergonomic handheld OCT angiography probe optimized for pediatric and supine imaging," Biomed Opt Express **10**(5), 2623 (2019).
10. S. Song, K. Zhou, J. J. Xu, Q. Zhang, S. Lyu, and R. Wang, "Development of a clinical prototype of a miniature hand-held optical coherence tomography probe for prematurity and pediatric ophthalmic imaging," Biomed Opt Express **10**(5), 2383 (2019).
11. F. Larocca, D. Nankivil, T. Dubose, C. A. Toth, S. Farsiu, and J. A. Izatt, "In vivo cellular-resolution retinal imaging in infants and children using an ultracompact handheld probe," Nat Photonics **10**(9), 580–584 (2016).
12. J. Yang, L. Liu, J. P. Campbell, D. Huang, and G. Liu, "Handheld optical coherence tomography angiography," Biomed Opt Express **8**(4), 2287 (2017).
13. Z. Duan, K. Huang, Z. Luo, K. Ma, G. Wang, X. Hu, J. Zhang, X. Luo, Y. Huang, G. Liu, X. Ding, P. Xiao, and J. Yuan, "Portable boom-type ultrahigh-resolution OCT with an integrated imaging probe for supine position retinal imaging," Biomed Opt Express **13**(6), 3295 (2022).
14. B. A. Scruggs, S. Ni, T.-T. P. Nguyen, S. Ostmo, M. F. Chiang, Y. Jia, D. Huang, Y. Jian, and J. P. Campbell, "Peripheral OCT Assisted by Scleral Depression in Retinopathy of Prematurity," Ophthalmology Science **2**(1), 100094 (2022).
15. T. Chan-Ling, G. A. Gole, G. E. Quinn, S. J. Adamson, and B. A. Darlow, "Pathophysiology, screening and treatment of ROP: A multi-disciplinary perspective," Prog Retin Eye Res **62**, 77–119 (2018).
16. T.-T. P. Nguyen, S. Ni, S. Ostmo, A. Rajagopalan, A. S. Coyner, M. Woodward, M. F. Chiang, Y. Jia, D. Huang, J. P. Campbell, and Y. Jian, "Association of Optical Coherence Tomography–Measured Fibrovascular Ridge Thickness and Clinical Disease Stage in Retinopathy of Prematurity," JAMA Ophthalmol **140**(11), 1121 (2022).
17. H. A. Mintz-Hittner, K. A. Kennedy, and A. Z. Chuang, "Efficacy of Intravitreal Bevacizumab for Stage 3+ Retinopathy of Prematurity," New England Journal of Medicine **364**(7), 603–615 (2011).
18. C. Gilbert, "Retinopathy of prematurity: A global perspective of the epidemics, population of babies at risk and implications for control," Early Hum Dev **84**(2), 77–82 (2008).
19. "Revised Indications for the Treatment of Retinopathy of Prematurity," Archives of Ophthalmology **121**(12), 1684 (2003).
20. "Multicenter Trial of Cryotherapy for Retinopathy of Prematurity," Archives of Ophthalmology **106**(4), 471 (1988).
21. S. J. Kim, A. D. Port, R. Swan, J. P. Campbell, R. V. P. Chan, and M. F. Chiang, "Retinopathy of prematurity: a review of risk factors and their clinical significance," Surv Ophthalmol **63**(5), 618–637 (2018).
22. S. Ni, X. Wei, R. Ng, S. Ostmo, M. F. Chiang, D. Huang, Y. Jia, J. P. Campbell, and Y. Jian, "High-speed and widefield handheld swept-source OCT angiography with a VCSEL light source," Biomed Opt Express **12**(6), 3553 (2021).
23. S. Ni, T.-T. P. Nguyen, R. Ng, S. Khan, S. Ostmo, Y. Jia, M. F. Chiang, D. Huang, J. Peter Campbell, and Y. Jian, "105° field of view non-contact handheld swept-source optical coherence tomography," Opt Lett **46**(23), 5878 (2021).
24. S. Ni, T. T. P. Nguyen, R. Ng, M. Woodward, S. Ostmo, Y. Jia, M. F. Chiang, D. Huang, A. H. Skalet, J. Peter Campbell, and Y. Jian, "Panretinal Optical Coherence Tomography," IEEE Trans Med Imaging **42**(11), 3219–3228 (2023).

25. X. Wei, T. T. Hormel, Y. Guo, and Y. Jia, "75-degree non-mydriatic single-volume optical coherence tomographic angiography," Biomed Opt Express **10**(12), 6286 (2019).
26. A. Camino, R. Ng, J. Huang, Y. Guo, S. Ni, Y. Jia, D. Huang, and Y. Jian, "Depth-resolved optimization of a real-time sensorless adaptive optics optical coherence tomography," Opt Lett **45**(9), 2612 (2020).
27. Y. Jian, K. Wong, and M. V. Sarunic, "Graphics processing unit accelerated optical coherence tomography processing at megahertz axial scan rate and high resolution video rate volumetric rendering," J Biomed Opt **18**(02), 1 (2013).
28. J. Xu, K. Wong, Y. Jian, and M. V. Sarunic, "Real-time acquisition and display of flow contrast using speckle variance optical coherence tomography in a graphics processing unit," J Biomed Opt **19**(02), 1 (2014).
29. Y. Jia, O. Tan, J. Tokayer, B. Potsaid, Y. Wang, J. J. Liu, M. F. Kraus, H. Subhash, J. G. Fujimoto, J. Hornegger, and D. Huang, "Split-spectrum amplitude-decorrelation angiography with optical coherence tomography," Opt Express **20**(4), 4710–4725 (2012).
30. X. Wei, T. T. Hormel, Y. Guo, T. S. Hwang, and Y. Jia, "High-resolution wide-field OCT angiography with a self-navigation method to correct microsaccades and blinks," Biomed Opt Express **11**(6), 3234–3245 (2020).
31. X. Wei, A. Camino, S. Pi, T. T. Hormel, W. Cepurna, D. Huang, J. C. Morrison, and Y. Jia, "Real-time cross-sectional and en face OCT angiography guiding high-quality scan acquisition," Opt Lett **44**(6), 1431–1434 (2019).
32. X. Chen, R. Imperio, C. Viehland, P. R. Patel, D. Tran-Viet, S. Mangalesh, S. G. Prakalapakorn, S. F. Freedman, J. A. Izatt, and C. A. Toth, "A pilot optical coherence tomography angiography classification of retinal neovascularization in retinopathy of prematurity," Sci Rep **14**(1), 568 (2024).
33. S. Ni, T.-T. P. Nguyen, R. Ng, S. Ostmo, Y. Jia, M. F. Chiang, D. Huang, A. H. Skalet, J. P. Campbell, and Y. Jian, "140° field-of-view contact handheld swept-source OCT for pediatric peripheral imaging," in *Ophthalmic Technologies XXXIII*, K. Bizheva, D. X. Hammer, and G. Schuele, eds. (SPIE, 2023), p. 54.
34. T.-T. P. Nguyen, S. Ni, S. Khan, X. Wei, S. R. Ostmo, M. F. Chiang, Y. Jia, D. Huang, Y. Jian, and J. P. Campbell, "Quantification of fibrovascular ridge thickness in retinopathy of prematurity using swept-source optical coherence tomography," Invest Ophthalmol Vis Sci **63**(7), 802-F0361 (2022).
35. S. Ni, T.-T. P. Nguyen, R. Ng, S. Khan, S. Ostmo, Y. Jia, M. F. Chiange, D. Huang, J. P. Campbell, and Y. Jian, "Ultra-widefield handheld swept-source OCT for peripheral retinal imaging," in *Ophthalmic Technologies XXXII*, D. X. Hammer, K. M. Joos, and D. V. Palanker, eds. (SPIE, 2022), p. 41.
36. S. Makita, M. Miura, S. Azuma, T. Mino, T. Yamaguchi, and Y. Yasuno, "Accurately motion-corrected Lissajous OCT with multi-type image registration," Biomed Opt Express **12**(1), 637 (2021).
37. S. Makita, S. Azuma, T. Mino, T. Yamaguchi, M. Miura, and Y. Yasuno, "Extending field-of-view of retinal imaging by optical coherence tomography using convolutional Lissajous and slow scan patterns," Biomed Opt Express **13**(10), 5212 (2022).
38. Y. Guo, T. T. Hormel, S. Pi, X. Wei, M. Gao, J. C. Morrison, and Y. Jia, "An end-to-end network for segmenting the vasculature of three retinal capillary plexuses from OCT angiographic volumes," Biomed Opt Express **12**(8), 4889 (2021).
39. Y. Guo, A. Camino, M. Zhang, J. Wang, D. Huang, T. Hwang, and Y. Jia, "Automated segmentation of retinal layer boundaries and capillary plexuses in wide-field optical coherence tomographic angiography," Biomed Opt Express **9**(9), 4429 (2018).